Influences of ENSO SST Anomalies and Winter Storm Tracks on the Interannual Variability of Upper-Troposphere Water Vapor over the Northern Hemisphere Extratropics

HUI WANG AND RONG FU

Institute of Atmospheric Physics, The University of Arizona, Tucson, Arizona

ABSTRACT

This study examines the interannual variability of winter upper-troposphere water vapor over the Northern Hemisphere using the National Aeronautics and Space Administration Water Vapor Project, the International Satellite Cloud Climatology Project data, and the European Centre for Medium-Range Weather Forecasting reanalysis. The El Niño–Southern Oscillation related tropical sea surface temperature (SST) anomalies dominate the upper-troposphere water vapor anomalies south of the climatological jet. The anomalies of baroclinic instability in the storm track regions, which relate to the Pacific–North American and the North Atlantic oscillation patterns, dominate those north of the climatological jet. The upper-troposphere water vapor increases in the eastern tropical Pacific, the Gulf of Mexico, and some areas of the North Atlantic with warmer tropical SST. It decreases in the subtropical and extratropical northeastern Pacific. Deep convection and vertical moisture fluxes dominate these changes. To the north of the climatological jet, stronger upper-level cyclonic flow dries the upper troposphere when the baroclinicity of the storm tracks is enhanced. Both vertical and meridional moisture transport contribute to these water vapor anomalies in the midlatitudes. High clouds, as a possible source/sink of water vapor, respond to the tropical SST anomalies and extratropical circulation in a pattern similar to the upper-troposphere water vapor, and they consequently positively correlate to the latter. In the Tropics and extratropics where high clouds are relatively abundant, water vapor concentration increases with temperature. Thus, the increase of evaporation or sublimation of high clouds probably contributes to the observed moistening of the upper troposphere, in addition to enhanced vapor transport. Conversely, in the subtropics where high clouds appear infrequently, water vapor concentration decreases with temperature, suggesting that the downward advection of drier air associated with subsidence dominates the drying of the upper troposphere.

1. Introduction

Water vapor in the cold upper troposphere has an effect comparable to that of the lower troposphere in determining the earth's outgoing longwave radiation (OLR), though it is only a small fraction of the total column moisture (Shine and Sinha 1991). Since what controls the lower-troposphere water vapor is relatively well understood, an inadequate understanding of water vapor in the upper troposphere (Lindzen 1990) becomes the main source of uncertainty in determining the water vapor feedbacks (Intergovernmental Panel on Climate Change 1995). What controls the upper-troposphere water vapor in the Tropics has been extensively studied through observations in the past decade (e.g., Stephens 1990; Rind et al. 1991; Sun and Lindzen 1993; Soden and Fu 1995; Bates et al. 1996; Newell et al. 1997; Liao

and Rind 1997). In contrast, much less effort has been given to understanding the distribution and variation of the upper-troposphere water vapor in the extratropics.

The specific humidity in the upper troposphere is lower over the extratropics than over the Tropics. The lower and middle troposphere over the extratropics also have colder temperatures and lower specific humidity than in the Tropics, and so are more "transparent" to infrared radiation emitted at the surface. Hence, OLR is as sensitive to the changes of the upper-troposphere humidity in midlatitude as over the Tropics (Thompson and Warren 1982; Lindzen 1997).

The processes responsible for the upper-troposphere water vapor distribution and variation in the extratropics differ from those in the Tropics in at least two ways. First, the extratropics have stronger horizontal gradients of humidity and pressure than the Tropics. The associated horizontal moisture transport could be as important as the vertical transport (Del Genio et al. 1994). Second, the net effect of deep convection on upper-troposphere water vapor is more difficult to estimate in the midlatitudes than in the Tropics. For example, while deep convection in the Pacific storm track region ap-

Corresponding author address: Dr. Rong Fu, Earth and Atmospheric Sciences, Georgia Institute of Technology, 221 Bobby Dodd Way, Atlanta, GA 30332-0340.
E-mail: fu@eas.gatech.edu

pears to moisten the upper troposphere (Hu and Liu 1998), the associated synoptic systems in other regions lead to the intrusion of stratospheric air (Price and Vaughan 1993) that dries the upper troposphere. Furthermore, the extratropical large-scale circulation not only depends on the atmospheric internal variability and extratropical ocean–atmosphere interaction, but it also responds to tropical sea surface temperature (SST) forcing (e.g., Dickinson 1971; Wallace and Gutzler 1981; Hoskins and Karoly 1981; Blackmon et al. 1983; Kumar and Hoerling 1995; Lau 1997; among others). While circulation patterns in the midlatitudes have been more thoroughly studied than the tropical dynamic processes, their impacts on the extratropical upper-troposphere water vapor have not been previously examined. An assessment of the latter would enable us to apply the well-developed theories of extratropical dynamics and tropical–extratropical interaction to an understanding of the distribution and variation of the midlatitude upper-troposphere water vapor.

In this study, we explore how the El Niño–Southern Oscillation (ENSO)-related tropical SST and the storm track–related extratropical circulation affect the interannual variability of the upper-troposphere water vapor over the Northern Hemisphere. Our ultimate goal is to understand the physical and dynamic processes responsible for the upper-troposphere water vapor variations. As the first step to approach this goal, we focus on the documentation of the interannual changes of upper-tropospheric humidity and their relationship to those of the tropical SST and extratropical circulation in this paper. In addition to anomalous water vapor and its fluxes, we also examine the relationship among high clouds, temperature, and the upper-troposphere water vapor, to infer how water phase change contributes to the vapor variability. Since clouds and water vapor are measured independently, results consistent with both observations would provide a higher level of confidence than would those obtained from a single dataset. This analysis is confined to the winter season, in order to more clearly diagnose the dynamic processes that govern the changes.

The datasets used in this study are described in section 2. The indexes for the ENSO SST and extratropical storm track circulation are defined in section 3. The empirical relationship between the upper-troposphere water vapor and tropical SST–extratropical circulation is analyzed in section 4. The relative importance of ENSO and storm tracks affecting the variability of the upper-troposphere water vapor is quantitatively examined. How water vapor transport and high clouds may contribute to the water vapor patterns is also discussed in Section 4. Discussion and conclusions are in Section 5.

2. The datasets

The data used in this study consist of monthly mean upper-troposphere water vapor, SST, 500–300-mb winds and geopotential height, and high cloud frequency of occurrence. The upper-troposphere water vapor is represented by the precipitable water between 500 and 300 mb, obtained from both the National Aeronautics and Space Administration (NASA) Water Vapor Project (NVAP; Randel et al. 1996) and the European Centre for Medium-Range Weather Forecasting (ECMWF) reanalyses (ERA). The SST is taken from the reconstructed Reynolds data (Smith et al. 1996) on a 2° lat × 2° long grid. The atmospheric fields are also from ERA on a 2.5° lat × 2.5° long grid over the Northern Hemisphere. As illustrated in Equations (1)–(3), moisture fluxes are first computed from 6-h instantaneous wind and specific humidity fields, and then averaged into a monthly mean. Thus, these fluxes are contributed by both mean and transient air flow. They are also weighted by areas they move across at each grid cell and air density. Hence, the zonal and meridional moisture fluxes ($\overline{uq}$, $\overline{vq}$) represent the amount of water vapor moving across a lateral wall extending from 500 to 300 mb along 2.5° lat for $\overline{uq}$ and 2.5° long for $\overline{vq}$. The vertical moisture flux ($\overline{wq}$) indicates the amount of water vapor moving across a horizontal area of 2.5° lat × 2.5° long at 500 mb:

$$\overline{uq} = \frac{1}{N} \sum_{n=1}^{N} \left[\sum_{i=1}^{3} \left(r_E \cdot \Delta\phi \cdot u_{i,n} \cdot q_{i,n} \cdot \frac{\Delta p_i}{g} \right) \right] \quad (1)$$

$$\overline{vq} = \frac{1}{N} \sum_{n=1}^{N} \left[\sum_{i=1}^{3} \left(r_E \cdot \cos\phi \cdot \Delta\alpha \cdot v_{i,n} \cdot q_{i,n} \cdot \frac{\Delta p_i}{g} \right) \right] \quad (2)$$

$$\overline{wq} = -\frac{1}{N} \sum_{n=1}^{N} \left(r_E^2 \cdot \cos\phi \cdot \Delta\alpha \cdot \Delta\phi \cdot \frac{\omega_{i,n} \cdot q_{i,n}}{g} \right), \quad (3)$$

where r_E denotes the radius of the earth, ϕ the latitude, α the longitude, and g the gravitational acceleration. Both $\Delta\phi$ and $\Delta\alpha$ are 2.5°. Pressure is 500 mb when $i = 1$ and 300 mb when $i = 3$, respectively. Further, n denotes the number of the 6-h temporal step at which instantaneous water vapor flux is computed such that $n = 1$ at the sixth UTC in the first day of the month. Also, $n = N$ at the 24th UTC in the last day of the month; N is the total number of temporal steps used in computing the monthly mean of the flux.

Here we use the data of the three winter months, that is, December–February (DJF), for the period of 1979 through 1993, with a total of 45 months. An anomaly is defined as the deviation from the corresponding 15-yr monthly average at each map cell over the Northern Hemisphere. Hence, both the 15-yr annual mean and seasonal cycle were removed prior to analysis. The observed high cloud cover was obtained from the International Satellite Cloud Climatology Project (ISCCP; Rossow et al. 1996) monthly mean cloud data (D2) for 16 winter months during January 1989–December 1993. The period of analysis related to high clouds is therefore limited to these 16 months.
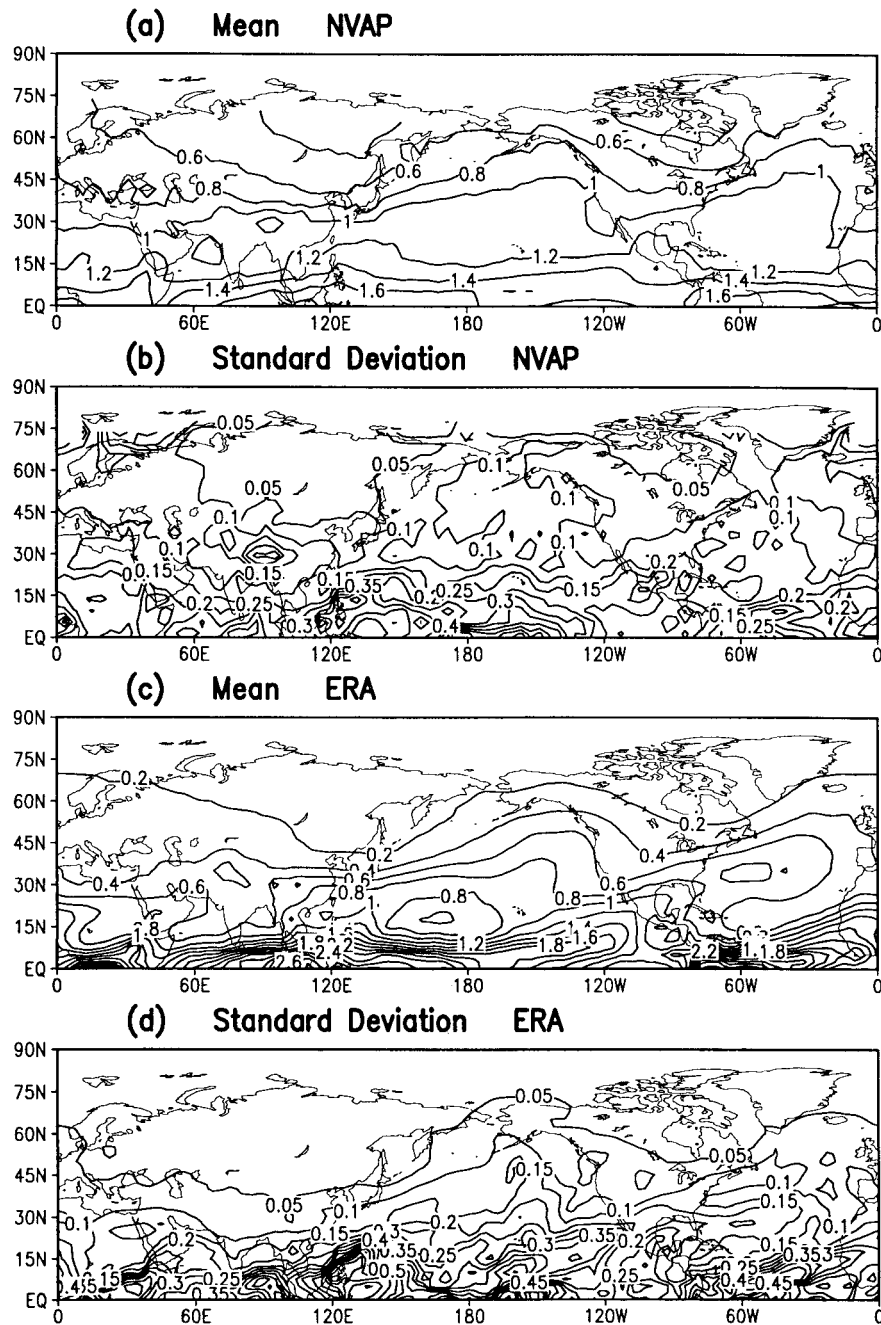
FIG. 1. Distribution of 5-yr (1988–92) winter monthly mean (Dec–Feb, DJF) 500–300 mb precipitable water [(a), (c)] and standard deviation [(b), (d)] over the Northern Hemisphere from the NVAP and ERA data, respectively. Contour intervals are 0.2 kg m^{-2} in [(a), (c)] and 0.05 kg m^{-2} in [(b), (d)].

3. Variabilities of upper-troposphere water vapor, tropical SST, and extratropical circulation

a. Variability of upper-troposphere water vapor over the Northern Hemisphere

The winter monthly mean 500–300-mb water vapor amount over the Northern Hemisphere is shown in Fig. 1a. The monthly means were obtained by averaging the NVAP layered (500–300 mb) precipitable water over December–February from 1988 to 1992, the only period available from NVAP. Areas with abundant upper-troposphere water vapor (>1.5 kg m^{-2}) are found in the Tropics, and over the North Pacific and North Atlantic (>1 kg m^{-2}), which are related to the wintertime ex-
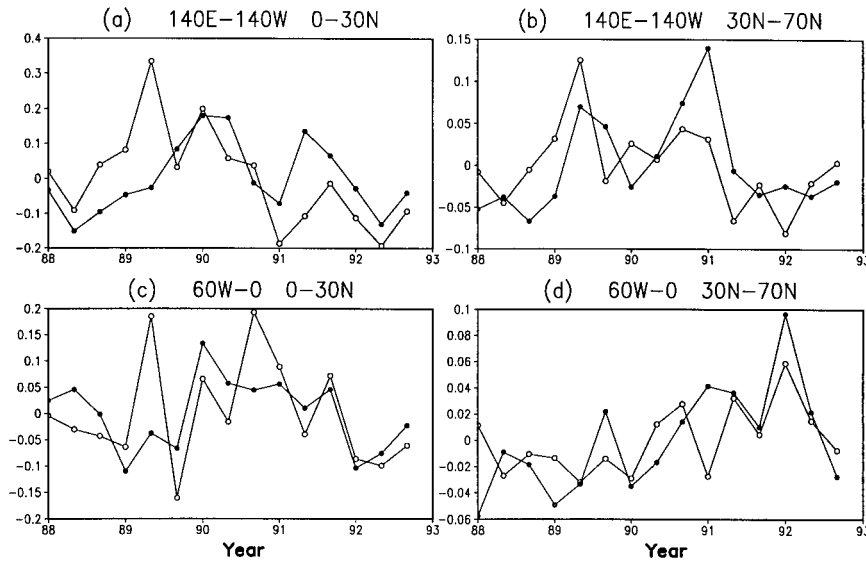
FIG. 2. Winter monthly mean 500–300-mb precipitable water anomalies averaged over (a) 0°–30°N and 140°E–140°W, (b) 30°–70°N and 140°E–140°W, (c) 0°–30°N and 60°W–0°, and (d) 30°–70°N and 60°W–0° both from NVAP (dot) and ERA (circle).

tratropical storm tracks. Figure 1b shows the standard deviation of the monthly mean precipitable water anomalies. In general, regions of high variability coincide with the regions of large monthly means. The standard deviation ranges from 0.3 to 0.5 kg m^{-2} over the Tropics. Over the extratropical oceans, it is of the order of 0.1 kg m^{-2}, twice as much as over the continents.

The corresponding monthly mean precipitable water and standard deviation derived from ERA data of the same period (Figs. 1c,d) show similar patterns of maximum and minimum water vapor mixing ratio to those from NVAP. However, mean precipitable water in ERA is greater than the NVAP over the Tropics and smaller over the extratropics, implying a stronger latitudinal gradient of upper-troposphere water vapor in ERA. Both standard deviations have the same orders of magnitude over most of the Northern Hemisphere, except for the extratropical North Pacific, where the variabilities in ERA are only about half those of NVAP. To ascertain the interannual variability of precipitable water in the two datasets, anomalous precipitable water averaged over the tropical–subtropical and extratropical regions of Pacific and Atlantic are shown in Fig. 2. In general, the temporal fluctuations exhibit similar interannual variability in the two datasets. Therefore, it is reasonable to employ the ERA data in the following analysis. ERA not only covers a longer period than NVAP, but also provides three-dimensional structure of humidity consistent with atmospheric wind and temperature fields.

b. Variability of tropical SST and extratropical circulation

To explore the possible connections between water vapor variability and tropical SST–extratropical atmo-

spheric circulation, several indexes (time series of anomalies) are constructed. The ENSO and associated tropical SST are one of the prominent sources of the interannual variability in the climate system. Thus, the averaged SST anomalies in the Niño 3.4 region (5°S–5°N, 170°–120°W; Climate Diagnostics Bulletin 1996) are used as an SST index (SSTI) of the tropical interannual variability and shown in Fig. 3a. The strong El Niño (1982/83 and 1991/92) and La Niña (1988/89) events are easily identified in this time series.

Ting et al. (1996) defined a zonal wind index (UI) as the difference between 500-mb zonal mean zonal winds at 35° and 55°N. They demonstrated that the variability of UI was largely independent of ENSO and that it could explain a large fraction of wintertime extratropical circulation variability. The correlation between UI (Fig. 3b) and SSTI in this study is 0.02. However, the major low-frequency circulation patterns in the atmosphere, for example, as classified by Barnston and Livezey (1987), have localized and zonally asymmetrical distributions that affect the patterns of water vapor anomalies. The UI, as a zonal mean variable, could underrepresent the extratropical variability of the upper-troposphere water vapor, for example, in the storm track regions.

Midlatitude synoptic systems affect moisture transport and cloud distribution, and hence water vapor distribution (e.g., Muller and Fuelberg 1990; Price and Vaughan 1993). The evolution of storm systems is closely related to jet stream and baroclinic instability. An accurate measure of baroclinicity is the Eady growth-rate maximum (Lindzen and Farrell 1980), defined as

$$BI = 0.31 f |\partial V / \partial z| / N,$$

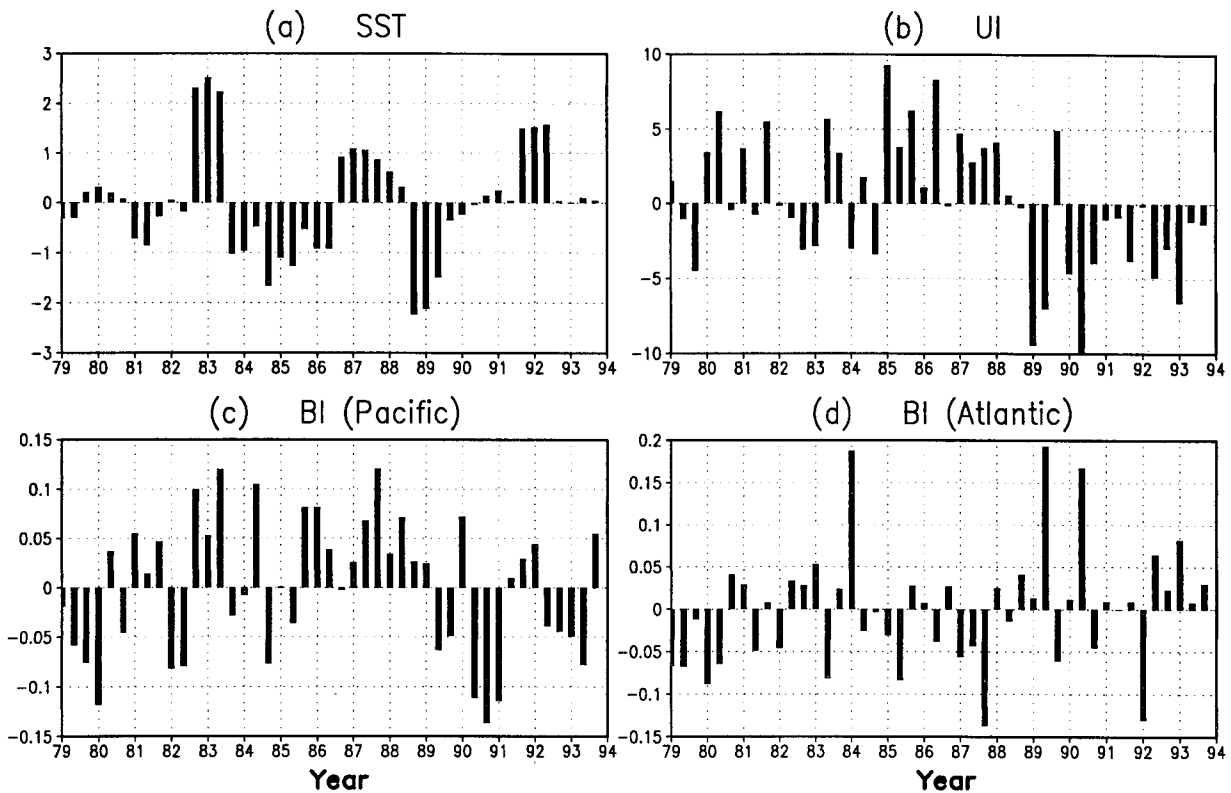where f is the Coriolis parameter, V the horizontal wind speed, and N the Brunt–Väisälä frequency. The param-

FIG. 3. Time series of four indexes: SSTI [(a), unit: °C], UI [(b), unit: m s^{-1}], BIp, and BIa [(c) and (d), unit: day^{-1}) for the winter months (DJF) of 1979–93.

eter was also used to study the maintenance of winter storm tracks by Hoskins and Valdes (1990). Their work shows that the baroclinicity parameter has maximum values over the Pacific and Atlantic jet regions. We therefore define two baroclinicity indexes (BIp and BIa) by averaging anomalous BI over the above-mentioned regions (30°–50°N, 140°E–140°W and 40°–60°N, 60°–0°W). The areas are chosen based on relatively high variability (standard deviation) and large mean values of BI (not shown). The BIp and BIa also highly correlate with two leading rotated BI EOF modes, suggesting that they represent the dominant variability of baroclinicity in the midlatitudes. The term $\partial V/\partial z$ was calculated based on winds at 850 and 700 mb. The two BI time series are shown in Figs. 3c and 3d. The correlation coefficient between BIp and UI is 0.38 and that between BIa and UI is −0.57. Thus, the variability of UI is partially attributable to the fluctuations of the Pacific and Atlantic jets, though the variations of the two jets are less correlated (−0.21).

A correlation of 0.24 is found between SSTI and BIp, and −0.20 between SSTI and BIa. Both exceed the 90% significance level. Therefore, associated with ENSO, there is a tendency of slightly stronger baroclinicity over the North Pacific and slightly weaker baroclinicity over the North Atlantic. Figure 3 also illustrates a strong persistence in anomalous SST through successive winter

months. In contrast, UI, BIa, and BIp show less month-to-month persistence. In most years, BIa and BIp display both positive and negative fluctuations through the three winter months.

The atmospheric circulation patterns, as represented by geopotential height at 300 mb, associated with the above four indices are plotted in Fig. 4. The anomalies of 300-mb height associated with SSTI exhibit a well-defined wave train (due to displacement of stationary troughs and ridges) over the Pacific–North American (PNA) regions, indicating the atmospheric response to the tropical SST forcing (e.g., Wallace and Gutzler 1981). The 300-mb height has strong correlation with UI throughout the Northern Hemisphere. The largest height gradients at 35° and 55°N indicate strong westerly and easterly geostrophic wind anomalies at the two latitudes, hence great values of UI. The correlation with BIp and BIa has more localized structures with centers of action over the PNA regions and the North Atlantic, respectively. The spatial distributions in Figs. 4c and 4d strongly resemble two dominant atmospheric circulation patterns: the PNA pattern and the North Atlantic oscillation (NAO) pattern (Barnston and Livezey 1987).

Both correlation of 300-mb height with SSTI and BIp (Figs. 4a,c) display a PNA-like pattern. However, the centers of the wave train–like anomalies locate differently. They are also independent of each other as sug-
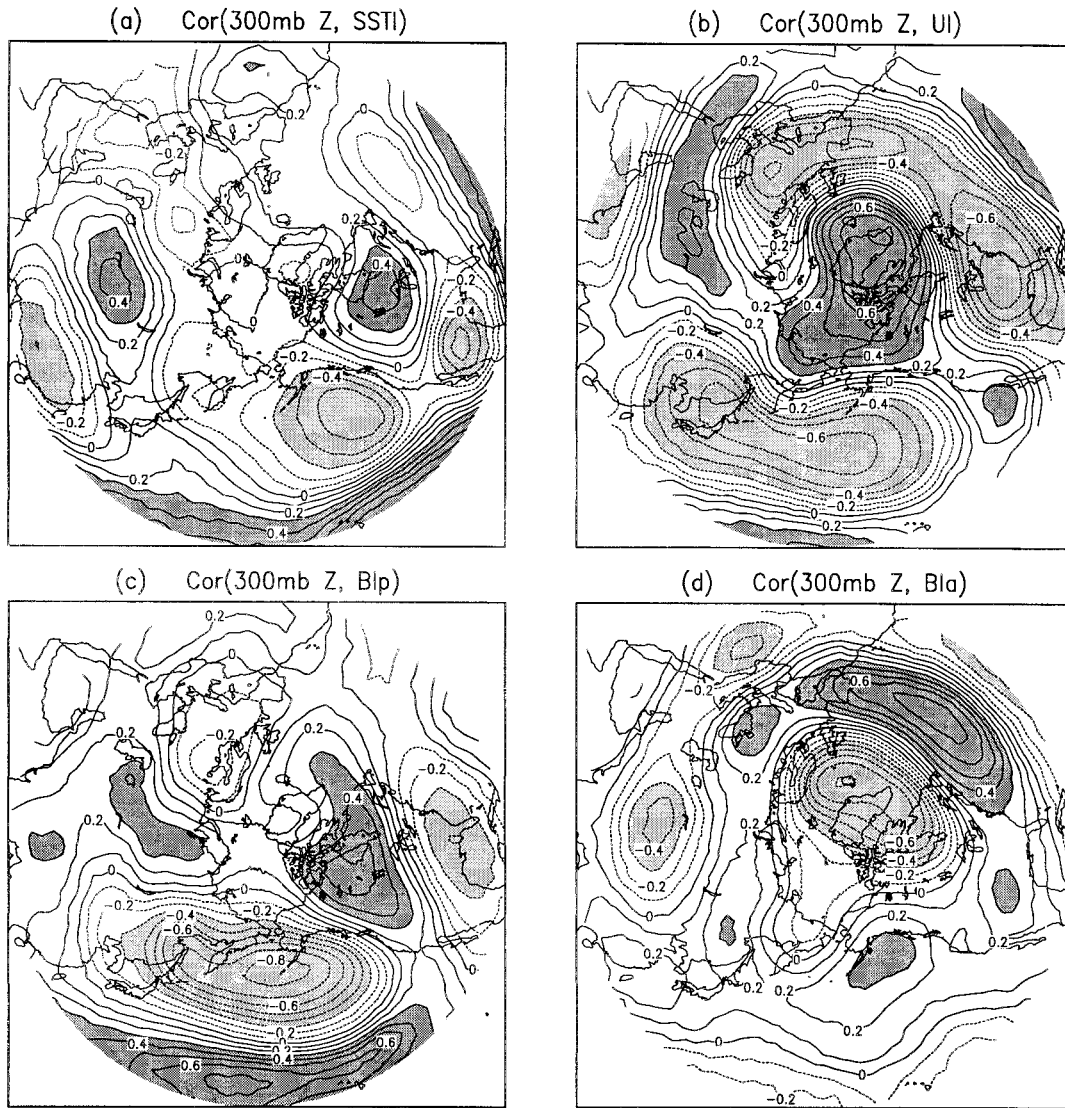
FIG. 4. Correlation of 15-yr (1979–93) winter monthly mean 300-mb height with (a) SSTI, (b) UI, (c) BIp, and (d) BIa, respectively. Contour interval is 0.1 and negative contours are dashed. Dark (light) shading indicates significant positive (negative) correlation (≥ 0.3 or ≤ -0.3).

gested by the poor correlation between SSTI and BIp. Furthermore, BIp is correlated to the North Pacific SST anomalies whose pattern (not shown) is very similar to the North Pacific mode characterized by Zhang et al. (1996). Their work revealed that the North Pacific SST mode is independent of tropical SST anomalies.

While SSTI is a good indication of the tropical SST variability, the construction of atmospheric indices is subject to arbitrary selection of both variable and domain for averaging. Whether the two baroclinicity indexes adequately capture the wintertime storm track and dominant extratropical circulation variability is examined by the singular value decomposition (SVD) method (Bretherton et al. 1992; Wallace et al. 1992), which objectively identifies pairs of spatial patterns with maximum temporal covariance between two fields. The SVD

analysis between Northern Hemisphere 300-mb height and the baroclinicity over the Pacific and over the Atlantic (not shown) reveal that the leading SVD mode of 300-mb height strongly resembles the circulation patterns in Figs. 4c and 4d, respectively. The two modes explain 56% of the covariance between the Northern Hemisphere 300-mb height and the baroclinicity over the Pacific, and 52% of the covariance between the Northern Hemisphere 300-mb height and the baroclinicity over the Atlantic. The SVD analysis confirms that both baroclinicity indices capture the coupled variability between the major wintertime storm tracks and the extratropical circulation. The results are also consistent with Lau (1988), who demonstrated that the variability of the wintertime storm tracks is associated with the PNA and NAO circulation patterns. Although the cir-
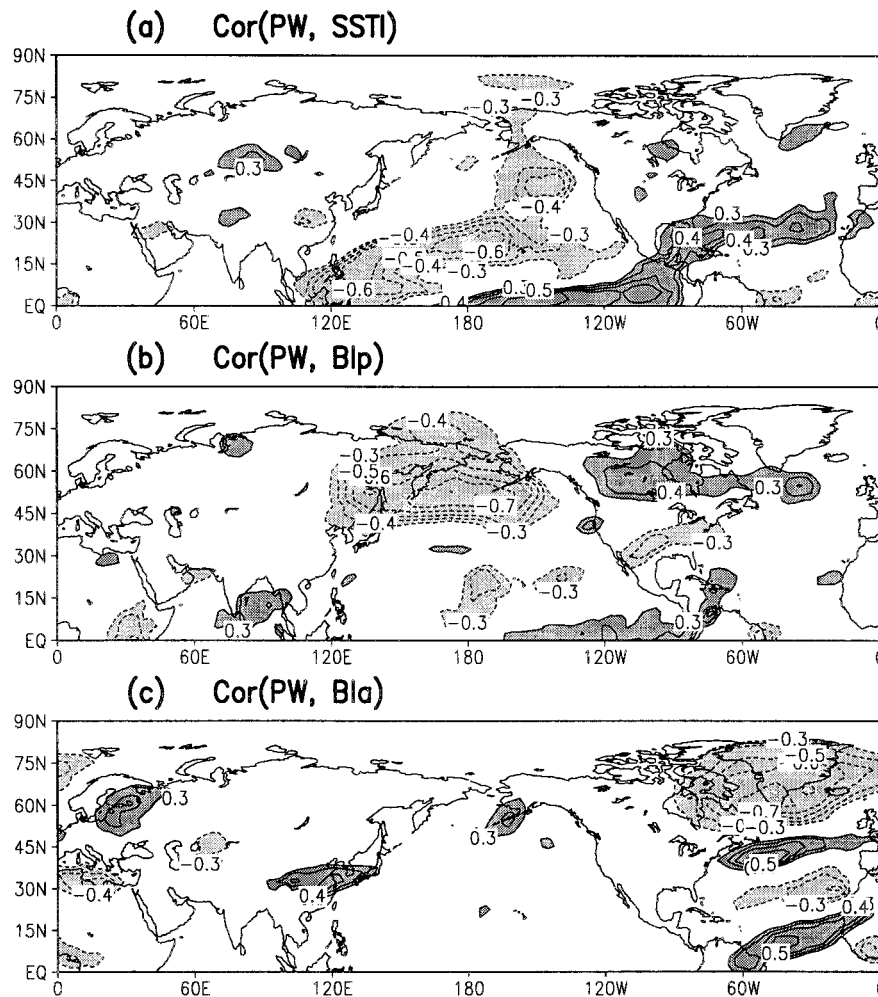
FIG. 5. Correlation of winter monthly mean 500–300-mb precipitable water with (a) SSTI, (b) BIp, and (c) BIa, respectively. Contours and shadings are the same as Fig. 4. Only contours exceeding 0.3 are given.

culation associated with UI (Fig. 4b) partially resembles both in Figs. 4c and 4d, the two BI indexes directly represent the atmospheric processes that affect the upper-troposphere water vapor and are therefore used in this analysis.

4. Relation of upper troposphere water vapor to the tropical SST and extratropical circulation

a. Variability of water vapor and its link to the tropical SST and extratropical circulation

Figure 5 shows the correlation of 500–300-mb precipitable water with SSTI, BIp, and BIa. Areas of significant positive correlation with SSTI are found over the eastern tropical Pacific, the Gulf of Mexico, and the North Atlantic around 30°N, and those of negative correlation are found over the western tropical Pacific and the subtropical and eastern North Pacific. Water vapor shows a significant correlation to BIp across the PNA

regions, with a broad drier area centered over the Aleutian Islands (40°–80°N, 120°E–140°W) and a large moistening area over Canada (50°–80°N, 30°–120°W), as BIp is higher than its climatological value. The correlation is very small over the climatological jet region. Associated with BIa, the water vapor displays several narrow bands of opposite sign correlation across the North Atlantic. Similar to the correlation with BIp, the strongest negative correlations are found to the north of the climatological jet, over Greenland, the Labrador Sea, and eastern Canada. Correlations with the three indices are generally small over Eurasia, where the interannual variabilities are small.

To determine the relative importance of tropical SST and extratropical atmospheric circulation to the upper-troposphere water vapor variability, Figs. 6a and 6b present the percentage of precipitable water variance explained by SSTI, BIp, and BIa, respectively, at each grid point calculated from ERA over 45 months. For
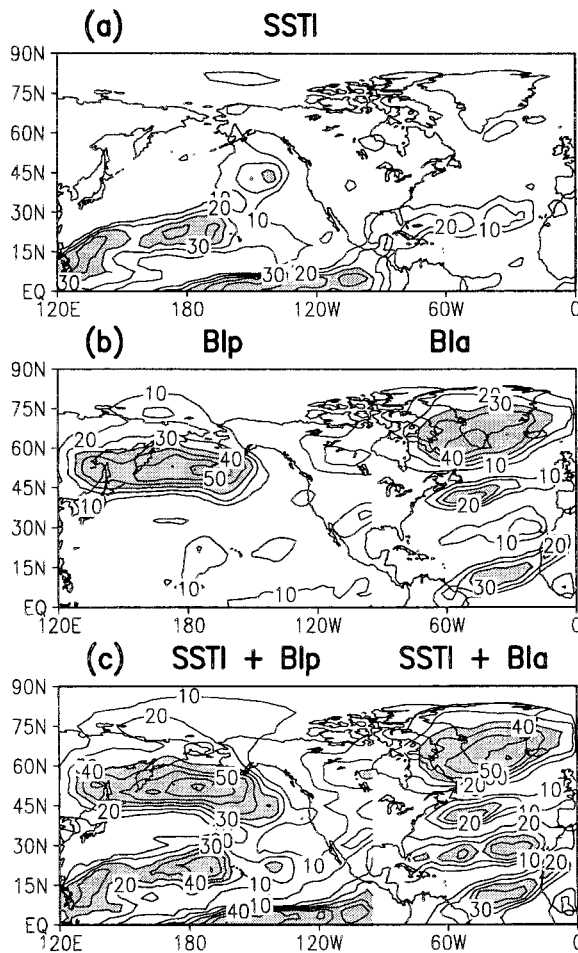
FIG. 6. Percentage of 500–300-mb precipitable water variance explained by (a) SSTI, (b) BIp over 120°E–90°W and BIa over 80°W–0°, and (c) combination of SSTI and BIp over 120°E–90°W, and combination of SSTI and BIa over 80°W–0°, respectively, over the 45 winter months in the ERA data. Contour interval is 10% and shading indicates the percentages greater than 30%.

each winter month, the precipitable water anomaly associated with the fluctuation of an index is obtained from the projection of that index amplitude on the corresponding linear regression map. The shaded areas in Fig. 6 indicate the values greater than 30%. Relatively high water vapor variability associated with SSTI is confined to the tropical and subtropical Pacific. In contrast, high water vapor variability associated with BIp and BIa occurs over midlatitudes, especially north of jet streams. The two indices account for more than 50% of the water vapor variance around the Aleutian Islands and Greenland, respectively. Averaging over the Tropics and subtropics (0°–30°N), SSTI explains 36% of the precipitable water variance, while BIp and BIa explain 19% and 15% of the variance, respectively. Over the extratropics (30°–90°N), 18% of variance is related to SSTI, 25% to BIp, and 20% to BIa. Figure 6c shows the percentages of the precipitable water variance explained by both SSTI and BIp over the Pacific, and that

explained by both SSTI and BIa over the Atlantic. The combined tropical SST and extratropical circulation variability accounts for a large fraction of the total upper-troposphere water vapor variations over the Northern Hemisphere.

b. How do changes in moisture transport and high cloud contribute to the water vapor variability?

Both changes in vapor transport and exchanges between its vapor and liquid–ice can cause the above changes in upper-troposphere water vapor. We examine how tropical SST anomalies and changes of storm tracks affect water vapor transport and high clouds, and how the latter may contribute to the observed changes of the upper troposphere water vapor in this section.

Figure 7 shows the vertically integrated (500–300 mb) anomalous horizontal moisture transport ($\delta \overline{uq}$, $\delta \overline{vq}$), obtained using the linear regression against one standard deviation fluctuation in each index. The shading indicates areas of anomalous upward moisture flux ($\delta \overline{wq} > 0$), and the contours in Figs. 7d–f indicate the anomalies of convective precipitation. The regions of upward moisture transport in Fig. 7a coincide with the positive correlation of precipitable water with SSTI in Fig. 5a. In the eastern tropical Pacific, the anomalous updraft is largely due to the SST-induced deep convection. Figure 7a also reveals a strong horizontal moisture transport from the eastern tropical Pacific to the North Atlantic. This suggests the existence of an upper-troposphere water vapor path over the subtropics during ENSO years. In the North Pacific, anomalous upper-level anticyclonic circulation occurs between 30° and 45°N in the western and central part, and anomalous cyclonic circulation occurs between 30° and 60°N in the eastern part when warmer SSTI occurs. Over the Atlantic ocean, the vectors of ($\delta \overline{uq}$, $\delta \overline{vq}$) indicate that the changes of the upper-level vapor transport are anticyclonic to the south and cyclonic to the north of 30°N. However, the strength of these circulation changes appears to be weaker than that associated with BIp and BIa.

Associated with BIp (Fig. 7b), the anomalous moisture fluxes are very similar to those associated with SSTI over the Gulf of Mexico and Gulf of Alaska. The largest difference between Figs. 7a and 7b is in the central North Pacific. There is a strong meridional moisture transport associated with the tropical SST variation, while in the same region strong zonal fluxes are associated with the storm track variability. The horizontal moisture fluxes in Fig. 7 are consistent with the corresponding large-scale circulation patterns in Fig. 4. For example, strong upper-anticyclonic anomalous flow is located around the anomalous high at 300 mb south of 45°N, and cyclonic anomalous flow appears around the anomalous low to the north of this latitude. The latter tends to demote the occurrence of extratropical cyclonic systems and may contribute to the observed dry anomalies associated with BIp north of the climatological jet
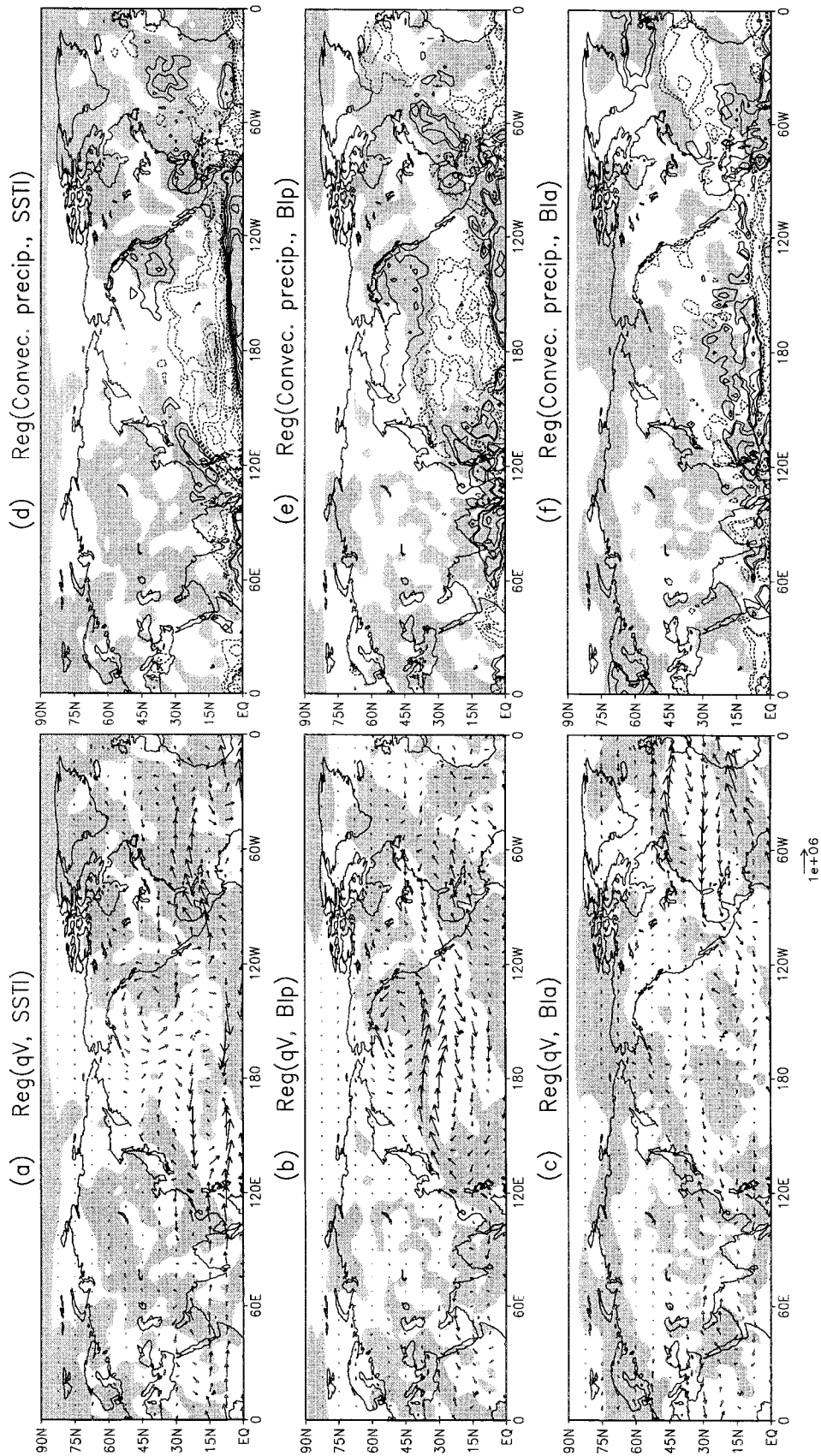
(d) Reg(Convec. precip., SSTI)

(e) Reg(Convec. precip., BIp)

(f) Reg(Convec. precip., BIa)

(a) Reg(qV, SSTI)

(b) Reg(qV, BIp)

(c) Reg(qV, BIa)

FIG. 7. Maps of linear regression between $\overline{\delta d\,uq}$ and $\overline{\delta uq}$ (vectors) based on one standard deviation departure and (a) SSTI, (b) BIp, and (c) BIa, and those between convective precipitation (contours) and (d) SSTI, (e) BIp, and (f) BIa, repectively. The shaded areas indicate the corresponding $\overline{\delta wq} > 0$. The unit is kg s^{-1}. The values of the contours are 0.1, 0.2, 0.5, 1.0, 1.5, and 2.0 mm day^{-1}.

(Fig. 5b). Associated with BIa (Fig. 7c), strong zonal moisture transport with upward motion occurs over the Atlantic climatological jet region. In general, all significant negative correlations in Fig. 5 are in the regions with subsidence and southward moisture fluxes in Fig. 7.

The influences of the three indices on the vertical moisture flux and the upper-troposphere water vapor distribution are examined in Fig. 8. The anomalous fluxes in several longitude–pressure cross sections are reconstructed from the linear regression of the zonal and vertical moisture fluxes against each index, to represent the changes correlated to each index. The latitudes at which the cross sections are made are determined according to either the strongest correlation of upper-troposphere water vapor with the relevant index (Fig. 5) or the locations of climatological jets. In addition, to further illustrate that the moistening is associated with anomalous upward flux and/or transport originating from the Tropics, Fig. 8 also shows the vertical structure of the changes associated with the three indices.

Associated with SSTI (Fig. 8a), specific humidity (dark shading) increases throughout the entire troposphere across the central and eastern Pacific at the equator. Clearly, the upward moisture fluxes associated with tropical deep convection contribute to the increase in water vapor. In the subtropics at 25°N (Fig. 8b), specific humidity increases significantly only in the upper level, although the water vapor path from the tropical Pacific to North Atlantic is found in both upper and lower levels. Both poleward (equatorward) and upward (downward) motions appear to contribute to the moistening (drying).

Stronger eastward moisture fluxes occur in the lower atmosphere over the climatological jet regions at 35°N when BIp (Fig. 8c) is greater and at 45°N when BIa becomes higher (Fig. 8e). Together with strong meridional fluxes as BIp increases, the westerly anomalies of moisture transport reflect the anomalous upper-level anticyclonic flow at 35°N (Fig. 8c) associated with BIp (Fig. 7b). Since this flow originates from the tropical western Pacific, it is reasonable to expect that those westerly anomalies of moisture transport moisten the upper troposphere over the North Pacific. Similarly, the westerly anomalies of moisture transport over North America and the Atlantic Ocean at 45°N (Fig. 8e) indicate an enhancement of moisture transport from the tropical Atlantic (Fig. 7c) and hence moistening of the upper troposphere at 45°N over the Atlantic Ocean when BIa increases (Fig. 8c). At 50° and 65°N (Figs. 8d,f), respectively, specific humidity decreases throughout the troposphere and hence displays a barotropic (altitude independent) structure. The water vapor deficiency is primarily accounted for by the downward and southward moisture fluxes, rather than by the zonal transport.

Figure 9 presents two meridional cross sections of water vapor fluxes associated with BIp and BIa at 180° and 30°W, respectively. The principal features are similar to those in Figs. 8d and 8f, showing that the down-draft and northerly winds accompany the negative water vapor anomalies induced by the midlatitude storm tracks. The results suggest that the changes in moisture transport contribute to, and possibly dominate, the observed changes of the upper-troposphere water vapor.

To determine whether the phase changes between vapor and liquid–ice also contribute to the observed upper-troposphere water vapor anomalies, we examine the correlation among the frequency of high clouds, the three indices (Fig. 10), and upper-troposphere water vapor anomalies (Fig. 11). Anomalies of high clouds are deduced from the ISCCP D2 dataset. The high clouds in this dataset consist of three types: cirrus, cirrostratus, and deep convective. The ISCCP data cover a spatial domain up to about 55°N. The correlation map associated with SSTI (Fig. 10a) resembles the water vapor pattern in Fig. 5a. The negative correlation over the western tropical Pacific and eastern North Pacific in Fig. 10a are largely contributed by cirrus cloud (not shown). Positive correlations over the central and eastern tropical Pacific, as well as over Mexico and the Gulf, are more related to cirrostratus and deep convective clouds. High clouds increase with BIp on the south side of the Pacific climatological jet entry (Fig. 10b) where anomalous updrafts occur (Fig. 7b). High clouds decrease over the Aleutian Islands, Alaska and surrounding areas, and the north side of the Pacific jet exit, where the negative water vapor anomalies occur (Fig. 5b).

The anomalous cloud pattern associated with BIa (Fig. 10c) reveals that high clouds decrease over Greenland and increase to the east where the winter storms associated with the NAO appear frequently (Rogers 1997). These variations of the high cloud with BIa over the Atlantic are consistent with that of the upper-troposphere water vapor in Fig. 5c. The high cloud patterns in Fig. 10 resemble their counterparts from the ERA data (not shown).

Figure 11a directly correlates the upper-troposphere water vapor to high clouds. The high cloud cover is positively correlated with the upper-troposphere water vapor, although with different magnitudes, over almost the entire hemisphere. Therefore, more upper-troposphere water vapor is associated with more extensive high clouds and hence greater total water amounts. This implies that the changes in large-scale circulation not only affect the upper-troposphere water vapor through direct vapor transport, but also change high clouds that probably further contribute to the upper-troposphere water vapor anomalies through water phase changes. To examine whether the changes of high clouds amplify or reduce the upper-troposphere water vapor anomalies, we analyze the correlation of 300-mb temperature with the specific humidity and relative humidity in Figs. 11b and 11c, respectively. Both specific humidity and relative humidity are significantly positively correlated with the temperature over the tropical Pacific and the midlatitudes across the Northern Hemisphere. Since warmer temperature enhances cloud evaporation, we suggest
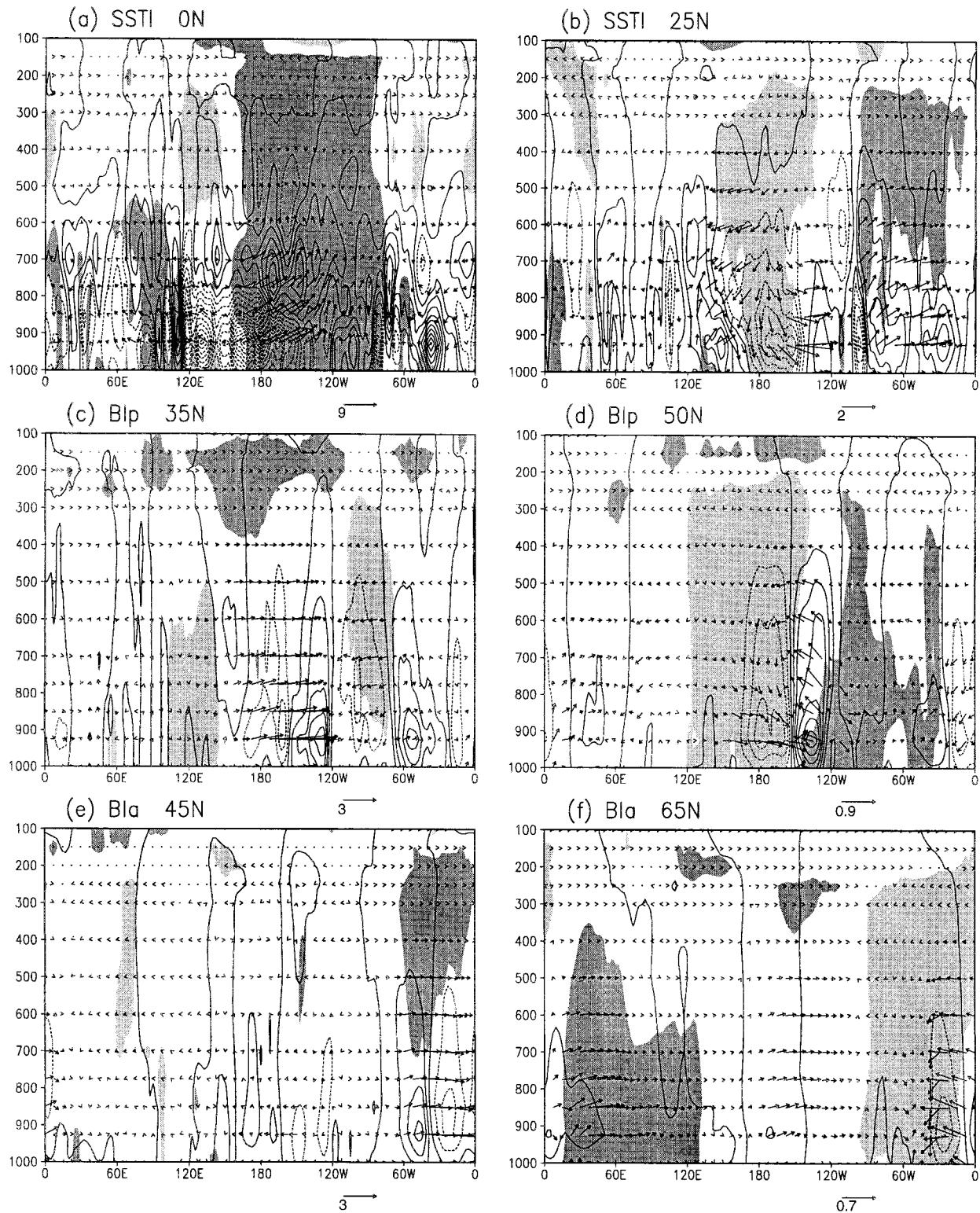
FIG. 8. Vertical cross section of $\overline{\delta uq}$ and $\overline{\delta wq}$ (vectors), and $\overline{\delta vq}$ (contours), obtained by linear regression of corresponding 15-yr winter monthly mean flux anomalies against one standard deviation fluctuations in SSTI, BIp, and BIa, respectively. The latitudinal location for each cross section is given at the top of that panel. The unit for $\overline{\delta uq}$ and $\overline{\delta vq}$ and $\overline{\delta wq}$ is 10^6 kg s^{-1}. For illustration purposes, the vector for $\overline{\delta wq}$ is amplified by a factor of 2. The contour interval is 2×10^5 (kg s^{-1}) for $\overline{\delta vq}$ and negative contours are dashed. Light and dark shadings indicate regions of specific humidity significantly (≤ -0.3 and ≥ 0.3) correlated with each of the indexes, respectively.
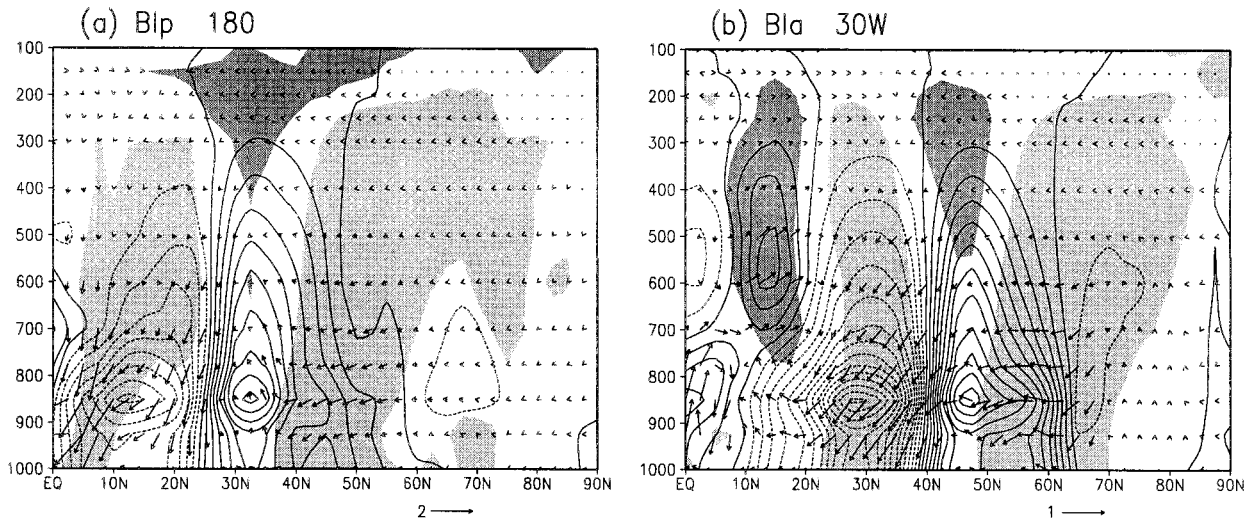
FIG. 9. Same as Fig. 8, but for meridional cross section of anomalous moisture fluxes $\overline{vq}$ and $\overline{wq}$ (vectors), and $\overline{uq}$ (contours) associated with (a) BIp at 180° and (b) BIa at 30°W. For illustration purpose, the vector for $\overline{wq}$ is amplified by a factor of 2. Contours and shadings are the same as Fig. 8.
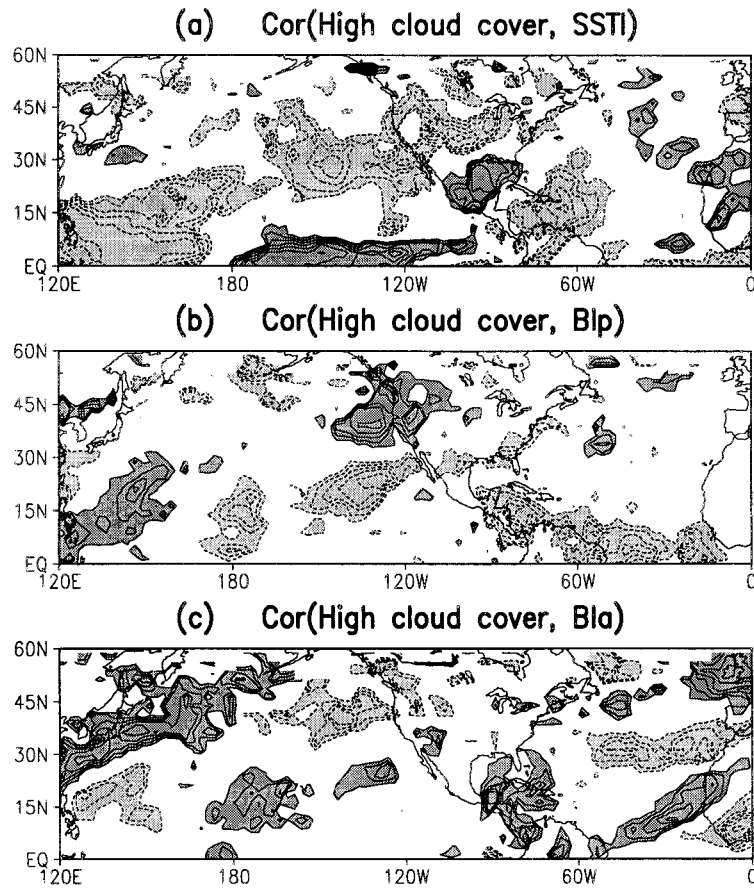

FIG. 10. Correlation of winter monthly mean (16 months) high cloud cover from ISCCP data with SSTI, BIp, and BIa, respectively. Contours and shadings are the same as Fig. 4. Only contours exceeding 0.3 are given.

(a)   Cor(High cloud cover, 500–300mb PW)

(b)   Cor(300mb q, 300mb T)
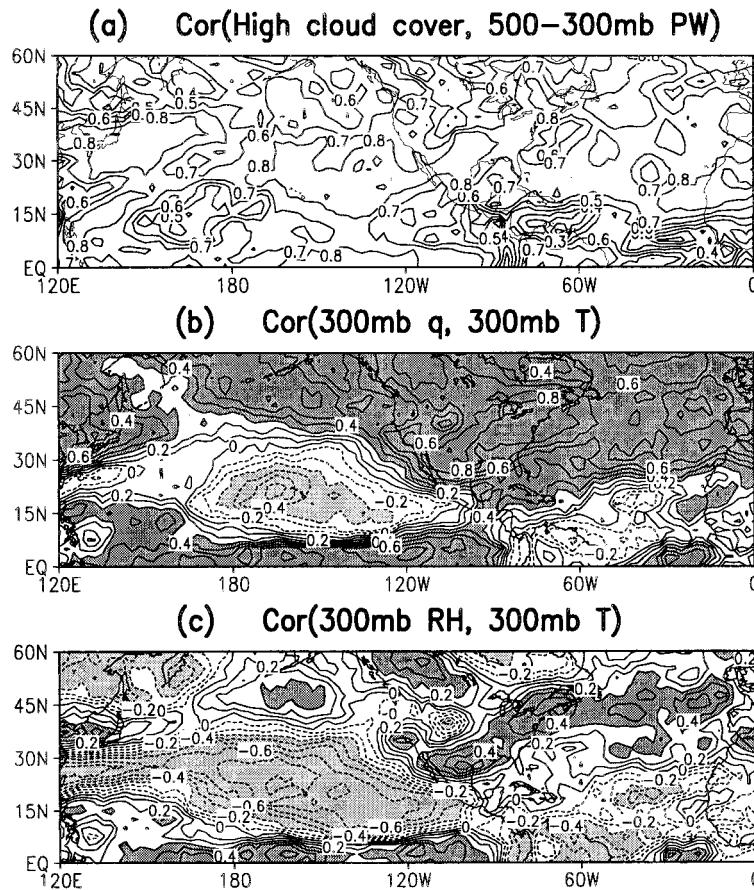

(c)   Cor(300mb RH, 300mb T)

FIG. 11. Correlation between high cloud cover and (a) 500–300 mb precipitable water, (b) 300-mb temperature and specific humidity, and (c) 300-mb temperature and relative humidity. All the variables are derived from ERA over 1979–93 winter months. Contour interval is 0.1, and negative contours are dashed. Dark (light) shading indicates significant positive (negative) correlation exceeding 0.3 in [(b), (c)].

that the latter also contributes to the observed increase of upper-troposphere water vapor, in addition to the vapor transport. Over the subtropical Pacific, both specific and relative humidity negatively correlate to temperature (Figs. 11b,c). Thus water vapor deficiency over this region results not from condensation, but from downward dry advection and adiabatic drying associated with subsidence, as shown in Figs. 8b and 9a.

5. Discussion and conclusions

This study addresses the effects of the ENSO-related tropical SST anomalies and changes of storm track–related extratropical circulation on the interannual variability of the wintertime upper-troposphere water vapor. The extratropical circulation changes associated with the well-defined PNA and NAO patterns are coupled with the variability of the Pacific and Atlantic storm tracks but are linearly independent of the tropical ENSO variation. We have demonstrated that both the tropical SST and the major winter storm tracks exert significant influences on the upper-troposphere water vapor variation.

The tropical SST associated with El Niño enhances tropical deep convection and extratropical baroclinicity through teleconnection. Consequently, warmer SST in the equatorial central and eastern Pacific increase the upper-troposphere water vapor over the tropical Pacific, the Gulf of Mexico, and some areas of the North Atlantic. Stronger baroclinicity in the storm track regions enhances upper-level anticyclonic flow and moistens the upper troposphere to the south of the climatological location of the jet. But it causes anomalous upper-level cyclonic flows to the north of the climatological jet and hence dries the upper troposphere there. The influence of the storm tracks over the midlatitudes is stronger than that of the tropical SST. This is a reflection of the existence of strong internal atmospheric variability in the midlatitudes (Kumar and Hoerling 1995; Ting et al. 1996).

Different atmospheric processes are involved in the changes in the upper-troposphere water vapor between the Tropics and the extratropics. In the Tropics, the variability of the upper-troposphere water vapor is largely due to the vertical moisture transport and deep convec-

tion. In the extratropics, both the vertical and meridional moisture transports associated with the storm track circulation are important, as previously suggested by Del Genio et al. (1994). The changes in evaporation/sublimation and condensation/deposition appear to be another source of the upper-troposphere water vapor anomalies over the tropical Pacific and midlatitudes where high clouds occur frequently. This mechanism, however, does not operate in the subtropics, where high clouds are infrequent. In the subtropical upper troposphere, drying (moistening) associated with a sinking (rising) motion appears to be the main cause of the upper-troposphere water vapor anomalies. Both water vapor and high clouds increase with enhanced poleward and upward water vapor transport. However, we cannot determine whether upper-troposphere water vapor anomalies are dominated by the direct vapor transport from a remote region or by the transport of liquid–ice from a remote region, which are then evaporated locally. Figure 8 also indicates that the influence of both tropical SST and extratropical circulation on the lower-troposphere water vapor is different from that on the upper troposphere.

Water vapor from ERA is strongly influenced by model parameterizations and is thus less reliable. Figure 1 shows that the variability of upper-troposphere water vapor in ERA is about half that in NVAP, despite a strong meridional gradient in the mean upper-troposphere humidity field. Hence, the interannual variability as indicated by ERA may be weaker than in reality. Incorporating high clouds from a different data source (ISCCP) in the analysis provides a validation of the results derived from the ERA data. The coherence between the satellite-observed response of high clouds and ERA upper-troposphere water vapor to the changes of the tropical SST–extratropical circulation indicates that the relationships between the upper-troposphere water vapor and tropical SST–extratropical circulation derived from ERA are not only statistically significantly but also qualitatively reasonable.

Trenberth (1990) has presented evidence of the wintertime surface temperature changes with decadal timescales over the Northern Hemisphere and deepening of the Aleutian low during 1977–88. He suggested that the advection of warm and moist air into Alaska (cold and dry air over the North Pacific) by the anomalous circulation is responsible for the increase (decrease) in temperature over that region. He further linked the deepened Aleutian low to the tropical El Niño events through teleconnection. The influence of tropical SST on the atmospheric PNA pattern with interdecadal variability is supported by the atmospheric general circulation model experiments (Kawamura et al. 1995). The circulation anomalies over the Gulf of Alaska and Aleutian Islands, as described in Trenberth (1990), also emerge in both Figs. 4a and 4b. We have noticed long-term trends of increase in upper-troposphere water vapor, SST, and circulation indexes in both tropics and extra-

tropics (not shown), especially associated with the NAO pattern. If these trends can be verified by more reliable observations, we could argue that the internal variability of extratropical circulation and its interaction with North Pacific SST may also contribute to the decadal changes in temperature. These decadal trends have not been removed in our analysis. How they affect the variability analyzed in this study and whether the SST and extratropical circulation influence the upper-troposphere water vapor on decadal or longer timescales have not been examined in this study.

This study focused on the water vapor variability from the general circulation perspective. Given the complexity of the processes controlling moisture transport in the atmosphere, it is also necessary to examine the water vapor changes associated with individual storms on synoptic timescales. We are currently conducting a more thorough diagnosis of the synoptic processes and their contribution to the interannual variability of the upper-troposphere water vapor in the extratropics.

REFERENCES

Barnston, A. G., and R. E. Livezey, 1987: Classification, seasonality and persistence of low-frequency atmospheric circulation patterns. *Mon. Wea. Rev.,* **115,** 1083–1126.

Bates, J. J., X. Wu, and D. L. Jackson, 1996: Interannual variability of upper-troposphere water vapor band brightness temperature. *J. Climate,* **9,** 427–438.

Blackmon, M. L., J. E. Geisler, and E. J. Pitcher, 1983: A general circulation model study of January climate anomaly patterns associated with interannual variation of equatorial Pacific sea surface temperatures. *J. Atmos. Sci.,* **40,** 1410–1425.

Bretherton, C. S., C. Smith, and J. M. Wallace, 1992: An intercomparison of methods for finding coupled patterns in climate data. *J. Climate,* **5,** 541–560.

Del Genio, A. D., W. Kovari Jr., and M.-S. Yao, 1994: Climatic implications of the seasonal variation of upper troposphere water vapor. *Geophys. Res. Lett.,* **21,** 2701–2704.

Dickinson, R. E., 1971: Cross-equatorial eddy momentum fluxes as evidence of tropical planetary wave sources. *Quart. J. Roy. Meteor. Soc.,* **97,** 554–558.

Hoskins, B., and D. Karoly, 1981: The steady linear response of a spherical atmosphere to thermal and orographic forcing. *J. Atmos. Sci.,* **38,** 1179–1196.

——, and P. J. Valdes, 1990: On the existence of storm tracks. *J. Atmos. Sci.,* **47,** 1854–1864.

Hu, H., and W. T. Liu, 1998: The impact of upper tropospheric humidity from Microwave Limb Sounder on the midlatitude greenhouse effect. *Geophys. Res. Lett.,* **25,** 3151–3154.

Intergovernmental Panel on Climate Change, 1995: *Climate Change.* J. T. Houghton, et al., Eds., Cambridge University Press, 572 pp.

Kawamura, R., M. Sugi, and N. Sato, 1995: Interdecadal and inter-annual variability in the northern extratropical circulation sim-ulated with the JMA global model. Part I: Wintertime leading mode. *J. Climate,* **8,** 3006–3019.

Kumar, A., and M. P. Hoerling, 1995: Prospects and limitations of seasonal atmospheric GCM predictions. *Bull. Amer. Meteor. Soc.,* **76,** 335–345.

Lau, N.-C., 1988: Variability of the observed midlatitude storm tracks in relation to low-frequency changes in the circulation pattern. *J. Atmos. Sci.,* **45,** 2718–2743.

——, 1997: Interactions between global SST anomalies and the mid-latitude atmospheric circulation. *Bull. Amer. Meteor. Soc.,* **78,** 21–33.

Liao, X., and D. Rind, 1997: Upper troposphere/lower stratosphere water vapor and troposphere deep convection. *J. Geophys. Res.,* **102,** 19 543–19 550.

Lindzen, R. S., 1990: Some coolness concerning global warming. *Bull. Amer. Meteor. Soc.,* **71,** 288–299.

——, 1997: Can increasing carbon dioxide cause climate change? *Proc. Nat. Acad. Sci.,* **94,** 8335–8342.

——, and B. Farrell, 1980: A simple approximation result for the maximum growth rate of baroclinic instabilities. *J. Atmos. Sci.,* **37,** 1648–1654.

Muller, B. M, and H. E. Fuelberg, 1990: A simulation and diagnostic study of water vapor image dry bands. *Mon. Wea. Rev.,* **118,** 705–722.

Newell, R. J., Y. Zhu, W. G. Read, and J. W. Waters, 1997: Rela-tionship between tropical upper troposphere moisture and eastern tropical Pacific sea surface temperature on an El Niño time scale. *Geophys. Res. Lett.,* **102,** 25–29.

Price, J., and G. Vaughan, 1993: The potential for stratosphere–tro-posphere exchange in cut-off-low systems. *Quart. J. Roy. Me-teor. Soc.,* **119,** 343–365.

Randel, D. L., T. H. Vonder Haar, M. A. Ringerud, G. L. Stephens, T. J. Greenwald, and C. L. Combs, 1996: A new global water vapor dataset. *Bull. Amer. Meteor. Soc.,* **77,** 1233–1246.

Rind, D., E. W. Chiou, W. Chu, J. Larsen, S. Oltmans, J. Lerner, M. P. McCormick, and L. McMaster, 1991: Positive water vapor feedback in climate models confirmed by satellite data. *Nature,* **349,** 500–503.

Rogers, J. C., 1997: North Atlantic storm track variability and its association to the North Atlantic Oscillation and climate vari-ability of Northern Europe. *J. Climate,* **10,** 1635–1647.

Rossow, W. B., A. W. Walker, D. E. Beuschel, and M. D. Roiter, 1996: International Satellite Cloud Climatology Project (ISCCP) documentation of new cloud datasets. World Meteorological Or-ganization, 115 pp.

Shine, K. P., and A. Sinha, 1991: Sensitivity of the Earth's climate to height-dependent changes in the water vapour mixing ratio. *Nature,* **354,** 382–385.

Smith, T. M., R. W. Reynolds, R. E. Livezey, and D. C. Stokes, 1996: Reconstruction of historical sea surface temperature using em-pirical orthogonal functions. *J. Climate,* **9,** 1403–1420.

Soden, B. J., and R. Fu, 1995: A satellite analysis of deep convection, upper troposphere humidity and the greenhouse effect. *J. Cli-mate,* **8,** 2333–2351.

Stephens, G. L., 1990: On the relationship between water vapor over the oceans and sea surface temperature. *J. Climate,* **3,** 634–645.

Sun, D. Z., and R. S. Lindzen, 1993: Distribution of tropical tro-posphere water vapor. *J. Atmos. Sci.,* **50,** 1643–1660.

Thompson, S. L., and S. G. Warren, 1982: Parameterization of out-going infrared radiation derived from detailed radiative calcu-lations. *J. Atmos. Sci.,* **39,** 2667–2680.

Ting, M., M. P. Hoerling, T. Xu, and A. Kumar, 1996: Northern Hemisphere teleconnection patterns during extreme Phases of the zonal-mean circulation. *J. Climate,* **9,** 2614–2633.

Trenberth, K. E., 1990: Recent observed interdecadal climate changes in the Northern Hemisphere. *Bull. Amer. Meteor. Soc.,* **71,** 988–993.

Wallace, J. M., and D. Gutzler, 1981: Teleconnection in the geopo-tential height field during the Northern Hemisphere winter. *Mon. Wea. Rev.,* **109,** 784–812.

——, C. Smith, and C. S. Bretherton, 1992: Singular value decom-position of wintertime sea surface temperature and 500-mb height anomalies. *J. Climate,* **5,** 561–576.

Zhang, Y., J. M. Wallace, and N. Iwasaka, 1996: Is climate variability over the North Pacific a linear response to ENSO? *J. Climate,* **9,** 1468–1478.